



# Interface charges redistribution enhanced monolithic etched copper foam-based Cu<sub>2</sub>O layer/TiO<sub>2</sub> nanodots heterojunction with high hydrogen evolution electrocatalytic activity



Bei Long<sup>a</sup>, Hao Yang<sup>b</sup>, Mingyang Li<sup>b</sup>, Muhammad-Sadeeq Balogun<sup>b</sup>, Wenjie Mai<sup>c</sup>, Gangfeng Ouyang<sup>b</sup>, Yexiang Tong<sup>a,b,\*,</sup>, Panagiotis Tsiakaras<sup>d,e,f,\*,</sup>, Shuqin Song<sup>a,\*,</sup>

<sup>a</sup> The Key Lab of Low-Carbon Chemistry & Energy Conservation of Guangdong Province, School of Materials Science and Engineering, Sun Yat-sen University, Guangzhou, 510275, China

<sup>b</sup> MOE of the Key Laboratory of Bioinorganic and Synthetic Chemistry, School of Chemistry, Sun Yat-sen University, Guangzhou, 510275, China

<sup>c</sup> Guangzhou Key Laboratory of Vacuum Coating Technologies and New Energy Materials, Guangdong Provincial Engineering Technology Research Center of Vacuum Coating Technologies and New Energy Materials, Department of Physics, Jinan University, Guangzhou 510632, China

<sup>d</sup> Laboratory of Materials and Devices for Electrochemical Power Industry, Ural Federal University, 19 Mira Str., Yekaterinburg, 620002, Russia

<sup>e</sup> Laboratory of Electrochemical Devices based on Solid Oxide Proton Electrolytes, Institute of High Temperature Electrochemistry (RAS), Yekaterinburg, 620990, Russia

<sup>f</sup> Laboratory of Alternative Energy Conversion Systems, Department of Mechanical Engineering, School of Engineering, University of Thessaly, Pedion Areos, 38834, Greece

## ARTICLE INFO

### Keywords:

Space-charge region  
p-n Heterojunction  
Interface charges redistribution  
Large-scale preparation of monolithic electrode  
Hydrogen evolution reaction

## ABSTRACT

Semiconducting materials are considered as excellent electrocatalysts for electrochemical water splitting; however, there is still a lack of relevant design and understanding of semiconducting composite electrodes.

Here, a monolithic electrode composed of etched copper foam and p-n heterojunction (p-type Cu<sub>2</sub>O layer and n-type TiO<sub>2</sub> nanodots with excellent hydrophilicity) is successfully prepared. This can reduce the electron transfer resistance, optimize water and H adsorption on catalyst surface and generate a space-charge region in phase interface, enhancing the local electrons density of Cu<sub>2</sub>O, which is proved by experimental results and density functional theory (DFT).

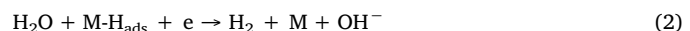
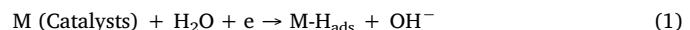
Owing to the whole accelerated Volmer-Heyrovsky pathway, the as-prepared heterojunction electrode exhibits low onset potential (18 mV), high electrocatalytic activity (a potential of 114 mV at 10 mA cm<sup>-2</sup>) and long-term stability for hydrogen evolution reaction in alkaline media that is comparable to that of Pt, enabling the large scale fabrication.

## 1. Introduction

The rapid consumption of fossil fuels leads to the accelerated environmental pollution and energy crisis [1–6]. Hydrogen fuel as a recyclable clean energy attracts an increasing and considerable attention of researchers [7–10]. Very recently, among all the methods, the electrochemical water splitting has been considered as a promising method to produce hydrogen fuel [11–15]. Moreover, the high cost and the scarcity of precious metal platinum resources with superior hydrogen evolution reaction (HER) have aroused scientific community's interest towards utilization of non-noble metal compounds [16–19]. Copper-based semiconductors (Cu<sub>2</sub>O, CuO and Cu(OH)<sub>2</sub> *et al.*) have, recently,

been adopted as active electrocatalysts for electrochemical water splitting mostly due to their low cost, environmentally friendly properties and excellent stability in alkaline media [20–23]. However, the large scale preparation of copper-based semiconductors with high electrocatalytic activity and long cycling-life in alkaline media still faces difficulties [21,24,25].

The typical process of hydrogen evolution reaction (HER) in alkaline media involves the following two steps (Volmer-Heyrovsky pathway) [26,27].



\* Corresponding author at: Laboratory of Alternative Energy Conversion Systems, Department of Mechanical Engineering, School of Engineering, University of Thessaly, Pedion Areos, 383 34, Greece.

\*\* Corresponding authors at: The Key Lab of Low-Carbon Chemistry & Energy Conservation of Guangdong Province, School of Materials Science and Engineering, Sun Yat-sen University, Guangzhou, 510275, China.

E-mail addresses: chedhx@mail.sysu.edu.cn (Y. Tong), tsiak@uth.gr (P. Tsiakaras), stsssq@mail.sysu.edu.cn (S. Song).

Obviously, these steps involve electrons transfer, demonstrating the importance of surface electron density of active sites in HER electrocatalysts; in other words, for the acceleration of the whole process enough electrons at the active sites are extremely important [26,28]. Moreover, from Eqs. (1) & (2) it can be deduced that a low  $H_2O$  adsorption free energy and an appropriate H adsorption free energy ( $\Delta G_{ads}$ ) on M are also essential for HER in alkaline media. It was reported that Schottky junction with a metal (serves the role of the p-type semiconductor) and a n-type semiconductor, which is a special case of p-n junction, can increase the surface electron density of metallic catalysts, thus boosting HER electrocatalytic activity [29]. While p-n heterojunctions with many similar properties to Schottky junction are more common and easily prepared [20,30–32]. Therefore, for the above reasons, it is trying to use the representative n-type  $TiO_2$ , with its excellent hydrophilicity, to modify the p-type  $Cu_2O$  semiconductor, facilitating the process of adsorbing water molecules and simultaneously changing electrons distribution on catalyst [33–35].

Herein, a monolithic etched copper foam-based  $Cu_2O$  layer/ $TiO_2$  nanodots composite (CFE- $Cu_2O/TiO_2$ ) is elaborately designed by the immersion and calcination process of etched copper foam to accelerate the whole Volmer-Heyrovsky process. First, the hydrophilic  $TiO_2$  attached on the etched electrode surface optimizes water adsorption free energy and decreases the interfacial resistance between electrocatalyst and electrolyte, promoting the Volmer step. Second, the formation of the p-n heterojunction results in the generation of a space-charge region and thereby an increased electrons density at local area of  $Cu_2O$ , and simultaneously accelerating the Volmer and Heyrovsky steps. Third,  $Cu_2O$  with the high electron density, can both activate the adsorbed H and possess the appropriate H adsorption free energy on catalyst, also in this way accelerating Heyrovsky steps. Therefore, the optimized electrode exhibits low onset potential, excellent electrocatalytic activity and attractive durability for HER in alkaline medium. Meanwhile, the simple preparation method enables the scaled-up electrode fabrication.

## 2. Experimental section

### 2.1. Preparation of etched copper foam

Copper foam ( $2.0\text{ cm} \times 3.0\text{ cm}$ ) was immersed in a mixed solution with  $2.5\text{ mol L}^{-1}$  KOH and  $0.125\text{ mol L}^{-1}$   $(NH_4)_2S_2O_8$  for 1 h ( $S_2O_8^{2-} + Cu \rightarrow 2SO_4^{2-} + Cu^{2+}$ ). The sample was taken out and washed with distilled water. Then, the as-prepared copper foam (dark blue) was soaked in  $0.1\text{ mol L}^{-1}$   $H_2SO_4$  for 10 min and washed in ultrasonic washer for 30 min, respectively, to remove the debris of surface. The as-obtained etched copper foam was dried in electric oven at  $60^\circ C$  and labeled as CFE.

### 2.2. Preparation of CFE- $Cu_2O$ , CFE- $TiO_2$ and CFE- $Cu_2O/TiO_2$

CFE (monolithic etched copper foam-based nanodots composite) was calcinated in a muffle furnace at  $300^\circ C$  for 1 h, which was denoted as CFE- $Cu_2O$ . The mass loading of  $Cu_2O$  is  $\approx 4\text{ mg cm}^{-2}$ . CFE was successively soaked in distilled water, ethanol, and  $0.2\text{ mol L}^{-1}$  aqueous titanium (IV) chloride solution for 1 min. The sample was then dried and heated on a hotplate at  $300^\circ C$  for 2 min. The immersion-heating process were repeated three times. Then, the resulting sample was calcinated in the muffle furnace at  $300^\circ C$  for 1 h. It should be noted that, when the drying and heating processes were carried out in Ar or in air atmosphere, the CFE- $TiO_2$  or the CFE- $Cu_2O/TiO_2$  sample was obtained, respectively. The content of  $TiO_2$  could be adjusted by controlling the time of immersion-heating process. The increased loading of  $TiO_2$  after the every immersion-heating process is  $\approx 0.4\text{ mg cm}^{-2}$ .

### 2.3. Characterization

To study the composition of materials, X-ray diffractometry (XRD,

D-MAX 2200 VPC, Rigaku), Raman spectroscopy (inVia, Renishaw) and X-ray photoelectron spectroscopy (XPS, ESCALab250, Thermo VG) were used. The morphologies were investigated by scanning electron microscopy (SEM, Gemini 500, Zeiss) and transmission electron microscopy (TEM, Tecnai™ G2 F30, FEI). Nitrogen adsorption/desorption isotherms were performed at  $77\text{ K}$  (ASAP 2020 V3.03 H) to get information about the specific surface area of electrodes. The contact angle between electrodes and water were tested in a contact-angle goniometer (DSA100, Kruss). Room-temperature photoluminescence (PL) spectra were obtained with a spectrofluorophotometer (RF-5301PC, Shimadzu).

### 2.4. Electrochemical tests

The electrochemical tests were performed in an electrochemical workstation (CHI760D) without iR correction. A three electrode system with Pt mesh ( $1.0\text{ cm}^2$ ) and saturated Ag/AgCl as the counter and reference electrode, respectively, was applied. The electrolyte was  $1.0\text{ mol L}^{-1}$  KOH aqueous solution. The active area of the working electrode was  $1.0\text{ cm}^2$ , which was fixed by the seal of epoxy resin. The polarization curves were taken from  $-1.0$  to  $-2.0\text{ V}$  (vs. Ag/AgCl) at  $10\text{ mV s}^{-1}$ . The potential values were counted by the following equation: Potential (vs. RHE) =  $E$  (vs. Ag/AgCl) +  $0.1976 + 0.0591 \times pH$ . The electrochemical stability tests were performed at 10, 50, and  $200\text{ mA cm}^{-2}$  under vigorous stirring for 24 h.

Electrochemical active surface area ( $S_{ESA}$ ) was calculated according to Eq. (3):

$$S_{ESA} = R_f S \quad (3)$$

where  $S$  amounts the geometric area of electrodes (here  $S = 1.0\text{ cm}^2$ ). The  $R_f$  is obtained by Eq. (4):

$$R_f = C_{dl}/20\text{ } \mu F\text{ cm}^{-2} \quad (4)$$

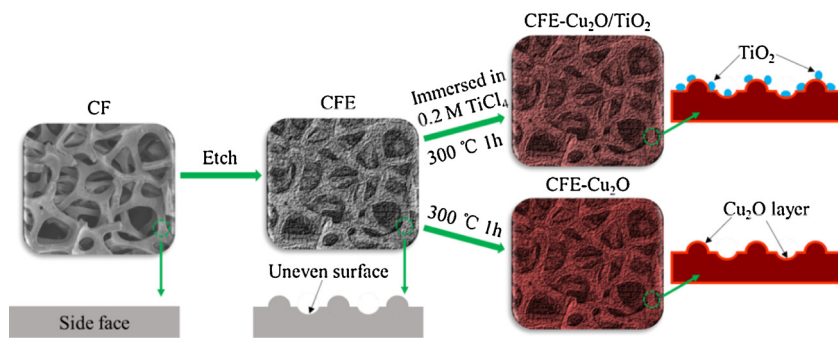
Eq. (4) describes the double-layer capacitance (denoted as  $C_{dl}$ ) of a smooth oxide surface ( $60\text{ } \mu F\text{ cm}^{-2}$ ) [36]; where  $C_{dl}$  is extracted from the cyclic voltammetry (CV) curves in a potential window between  $0.1$ – $0.2\text{ V}$  (vs. RHE) in  $1.0\text{ mol L}^{-1}$  KOH. The CV curves were recorded at different scan rates (5, 10, 20, 50, 100 and  $200\text{ mV s}^{-1}$ ).  $C_{dl}$  was calculated by plotting the  $j_a-j_c$  difference at  $0.15\text{ V}$  (vs. RHE) (where  $j_a$  and  $j_c$  are the anodic and cathodic current density respectively) against the scan rate, in which the slope was the double of  $C_{dl}$ .

### 2.5. Density functional theory calculations

The calculation model of reaction process referring to HER over  $Cu_2O$ ,  $TiO_2$  and  $Cu_2O/TiO_2$  composite, was realized by the aid of density functional theory (DFT) (using the Vienna Ab-initio Simulation Package). For DFT calculation, the (111) phase of  $TiO_2$  (JCPDS no. 65-0190) and the (111) phase of  $Cu_2O$  (JCPDS no. 65-3288) were used. The cutoff energy of plane wave was 500 eV. For Perdew-Burke-Ernzerhof form, the generalized-gradient approximation was used. A projector augmented wave approach (a technique used in *ab-initio* electronic structure calculation) also was applied [37]. In the process of geometric optimization of  $TiO_2$  and  $Cu_2O$  single layers, the Brillouin zones were sampled with  $5 \times 5 \times 1$  and  $3 \times 3 \times 5$  mesh. The computation of densities of states (DOS) was performed by a denser k-points grid of  $9 \times 9 \times 1$  size. A  $20\text{ \AA}$  thickness of vacuum space was used. The change of Gibbs free energy ( $\Delta G$ ) in each reaction process was calculated by using Gibbs equation (Eq. (5)).

$$\Delta G = E_{tot(b)} - E_{tot(a)} + \Delta E_{ZPE} - T\Delta S \quad (5)$$

Where  $E_{tot(b)}$  is the energy of intermediate at the latter state,  $E_{tot(a)}$  is the energy of intermediate at the previous status,  $\Delta S$  and  $\Delta E_{ZPE}$  can be obtained by calculating the entropy change and the zero point energy change of the intermediates at previous and latter state respectively.



**Scheme 1.** Schematic illustration procedure of CFE-Cu<sub>2</sub>O and CFE-Cu<sub>2</sub>O/TiO<sub>2</sub>.

### 3. Results and discussion

#### 3.1. Electrode preparation and characterization

The preparation process of the monolithic CFE-Cu<sub>2</sub>O/TiO<sub>2</sub> is schematically described below:

The etched copper foam-based Cu<sub>2</sub>O layer/TiO<sub>2</sub> nanodots composite can be prepared by the initial etching process followed by the repetition of the immersion and calcination steps (**Scheme 1**). The specific preparation process can be seen in experimental section.

The compositions and morphologies of CF, CFE-Cu<sub>2</sub>O and CFE-Cu<sub>2</sub>O/TiO<sub>2</sub> are initially studied by XRD, XPS, BET, SEM and TEM measurements. The untreated CF and CFE only exhibit strong metal copper peaks (JCPDS 04-0836) as seen in Figs 1 a and S1. After calcination, i.e., forming CFE-Cu<sub>2</sub>O, the oxidation of superficial copper leads

to the generation of a Cu<sub>2</sub>O layer (JCPDS 65-3288).

However, the characteristic peaks of TiO<sub>2</sub> cannot be detected in CFE-Cu<sub>2</sub>O/TiO<sub>2</sub>. The XRD profile of pure TiO<sub>2</sub>, recorded over the aqueous titanium (IV) chloride solution and calcinated at 300 °C in air, indicates its low crystallinity (**Fig. 1b**), which explains the non-detection of the characteristic peaks of TiO<sub>2</sub> in the XRD pattern of CFE-Cu<sub>2</sub>O/TiO<sub>2</sub>. The high-resolution Ti 2p and O 1s XPS spectra prove the existence of TiO<sub>2</sub>. The strong Ti 2p peaks at 458.01 and 463.88 eV, which correspond to Ti<sup>4+</sup> in CFE-Cu<sub>2</sub>O/TiO<sub>2</sub>, can be detected compared to the negligible signals of CFE-Cu<sub>2</sub>O (**Fig. 1c**) [38,39]. The O 1s spectra of CFE-Cu<sub>2</sub>O can be divided into two peaks at 529.70 and 531.40 eV attributed to typical O–Cu and O–H bonds (Fig. S2) [40,41]. While a new peak resulting from O–Ti bond can be found in O 1s spectra of CFE-Cu<sub>2</sub>O/TiO<sub>2</sub>, also suggesting the existence of TiO<sub>2</sub>. As shown in **Fig. 1d**, after suitable chemical erosion, the pore volume and specific surface

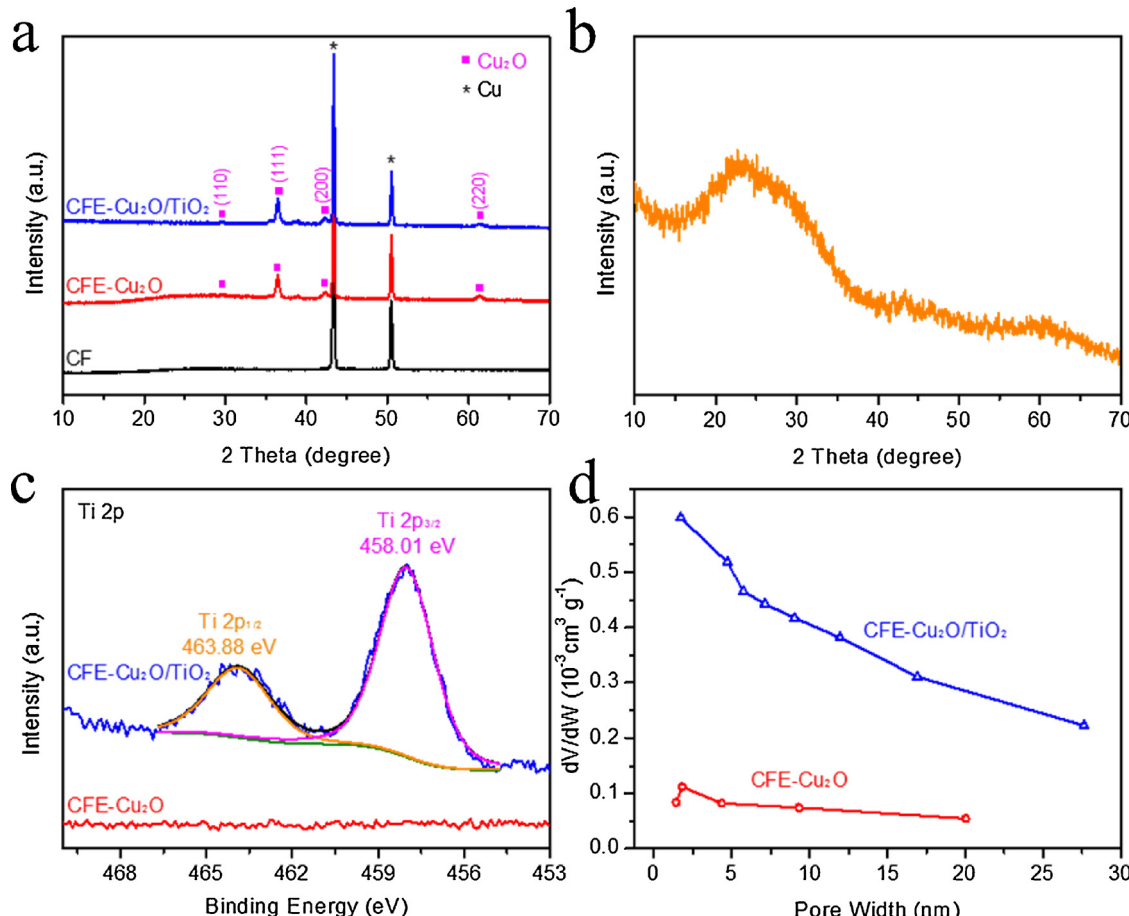


**Fig. 1.** (a) XRD patterns of CF, CFE-Cu<sub>2</sub>O and CFE-Cu<sub>2</sub>O/TiO<sub>2</sub>. (b) XRD pattern of TiO<sub>2</sub>. Ti 2p XPS spectra (c) and pore width distribution (d) of CFE-Cu<sub>2</sub>O and CFE-Cu<sub>2</sub>O/TiO<sub>2</sub>.

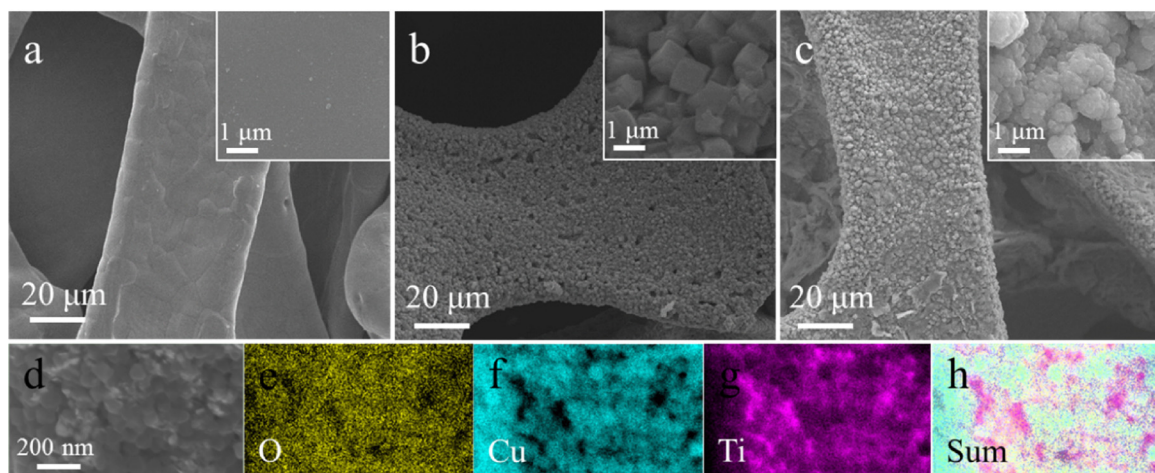


**Fig. 2.** SEM images of CF (a), CFE-Cu<sub>2</sub>O (b) and CFE-Cu<sub>2</sub>O/TiO<sub>2</sub> (c). (d-h) Elemental mappings of O, Cu and Ti in CFE-Cu<sub>2</sub>O/TiO<sub>2</sub>.

area of CF are markedly enhanced. The pore volume and specific surface area of CFE (CF) are 0.000595 (0.000240) cm<sup>3</sup> g<sup>-1</sup> and 0.8207 (0.5955) m<sup>2</sup> g<sup>-1</sup>, respectively. The larger specific surface area of CFE is beneficial to the generation of active materials (Cu<sub>2</sub>O) and the increment of active sites.

SEM images reveal the obvious modification of chemical erosion for the superficial morphology of CF. The pristine CF presents a smooth surface, while the surface of CFE is uneven and obviously exhibits many holes (Figs 2 a and S3), explaining the reason for its increased specific surface area and pore volume. After the CFE calcination in air, the morphology of CFE-Cu<sub>2</sub>O keeps unchanged (Fig. 2b). The uneven surface of CFE-Cu<sub>2</sub>O/TiO<sub>2</sub> will be covered with a film of small particles after the CFE is soaked in the aqueous titanium (IV) chloride solution (Fig. 2c) followed by calcination in air. According to high-resolution TEM image (Fig. S4), the size of TiO<sub>2</sub> is 10–20 nm and the interplanar spacings of 0.205 and 0.219 nm are ascribed to (210) and (111) phase of TiO<sub>2</sub> (JCPDS no. 65-0190). In addition, TiO<sub>2</sub> nanoparticle can be observed in TEM images of CFE-Cu<sub>2</sub>O/TiO<sub>2</sub> (Fig. S5). The clear lattice fringes with the interplanar spacings of 0.246 and 0.219 nm belong to (111) phase of Cu<sub>2</sub>O and (111) phase of TiO<sub>2</sub>. Energy dispersive X-Ray spectroscopy (EDX) maps show the elemental distribution of O, Cu and Ti on CFE-Cu<sub>2</sub>O/TiO<sub>2</sub> (Figs 2d–h), further proving the successful growth of TiO<sub>2</sub> on the surface of Cu<sub>2</sub>O.

To determine the effect of TiO<sub>2</sub> on the physical and chemical properties of Cu<sub>2</sub>O, the existence of a space-charge region is firstly proved, which is accompanied by the generation of the build-in electric field and the band bending [29]. Accordingly, the band bending reflected by the improved separation efficiency of photo-generated electrons and holes pair can confirm the existence of the space-charge region [35,41,42]. The photoluminescence (PL) spectra with an excitation wavelength of 330 nm and the photocurrent at open circuit voltage are recorded, and the results are shown in Fig. 3a.

The emission peak at 441 nm of CFE-Cu<sub>2</sub>O/TiO<sub>2</sub> is weaker than that of CFE-Cu<sub>2</sub>O, suggesting that the photoelectrons of Cu<sub>2</sub>O tend to be transferred at the TiO<sub>2</sub> and the separation of electrons and holes can be improved [35,42]. Meanwhile, in view of the narrow light absorption range of TiO<sub>2</sub>, the stronger photocurrent of CFE-Cu<sub>2</sub>O/TiO<sub>2</sub> can also be attributed to the oriented electron transfer (inset of Fig. 3a) [42]. Furthermore, compared to CFE-Cu<sub>2</sub>O, the enhanced charge injection efficiency of CFE-Cu<sub>2</sub>O/TiO<sub>2</sub> proves the reduction in the recombination process (Fig. S6) [43,44]. The above electron transfer is due to the band bending of semiconductors, thus verifying the existence of the space-charge region [34,41]. The high-resolution Cu 2p XPS spectra and Raman spectra supply strong evidences for the charge density change on CFE-Cu<sub>2</sub>O/TiO<sub>2</sub>. The characteristic peaks of CFE-Cu<sub>2</sub>O/TiO<sub>2</sub> shift to a lower binding energy compared to those of CFE-Cu<sub>2</sub>O in Cu 2p XPS

spectra of Fig. 3b ( $\Delta E = 0.21$  eV), indicating the increased electrons density on the surface of Cu<sub>2</sub>O [29]. To identify the Cu<sup>+</sup> in Cu<sub>2</sub>O, Auger electron spectra are studied (Fig. S7). The characteristic peaks at 916.84 and 916.09 eV are ascribed to Cu<sup>+</sup> [8,45]. A peak shifting toward low binding energy of CFE-Cu<sub>2</sub>O/TiO<sub>2</sub> can also be distinguished. Meantime, both the peaks at 107.4, 147.8 and 218.1 cm<sup>-1</sup>, relative to the Cu-O bond in the Raman spectra of CFE-Cu<sub>2</sub>O and the positive red-shifts of the Cu-O bond in CFE-Cu<sub>2</sub>O/TiO<sub>2</sub>, can be seen, also suggesting the strong electronic interaction between TiO<sub>2</sub> and Cu<sub>2</sub>O in the heterojunction (Fig. 3c) [26,45,46].

The density functional theory (DFT) calculation results further prove the increased electron density of Cu<sub>2</sub>O in CFE-Cu<sub>2</sub>O/TiO<sub>2</sub> (Fig. 3d), while the computational model can be seen in Fig. S8. Compared to the individual Cu<sub>2</sub>O, the electron densities of Cu and O in heterojunction increase. On the contrary, the electron densities of Ti and O in heterojunction decrease. Therefore, it is demonstrated that the space-charge region in the heterojunction phase interface leads to the electrons movement; many of these electrons are focused on the local area of Cu<sub>2</sub>O and thus gradually evolving into active-sites. The hydrophilicity of electrode related to water adsorption energy has a great influence on the electrode and electrolyte contact. The good hydrophilicity suggests that more active sites can keep good contact with electrolyte and decreases the interfacial resistance, therefore prompting the electrochemical reaction rate between electrode and water [46]. As displayed in Fig. 3e, the value of contact angle of water on the surface of CFE-Cu<sub>2</sub>O is 135°, which is not good for the water adsorption [47]. After the modification of TiO<sub>2</sub>, with good hydrophilicity, the contact angle of CFE-Cu<sub>2</sub>O/TiO<sub>2</sub> is reduced to 17° (Fig. 3f). When CFE-Cu<sub>2</sub>O and CFE-Cu<sub>2</sub>O/TiO<sub>2</sub> are immersed into water, CFE-Cu<sub>2</sub>O will rise to the surface, while there is an opposite phenomenon for CFE-Cu<sub>2</sub>O/TiO<sub>2</sub>, also demonstrating the better hydrophilicity of CFE-Cu<sub>2</sub>O/TiO<sub>2</sub> (Fig. S9). Meanwhile, DFT calculations reveal that the water absorption free energy of Cu<sub>2</sub>O/TiO<sub>2</sub> is much less than those of Cu<sub>2</sub>O and TiO<sub>2</sub> (inset of Fig. 3f), which confirms the improved Volmer step on CFE-Cu<sub>2</sub>O/TiO<sub>2</sub>.

### 3.2. Electrochemical tests

Nyquist plots (Fig. 4a) show the dramatically decreased charge transfer resistance of CFE-Cu<sub>2</sub>O/TiO<sub>2</sub>. The resistance of CFE-Cu<sub>2</sub>O/TiO<sub>2</sub> is 6.0 Ω, while that of CFE-Cu<sub>2</sub>O is 12.0 Ω, explaining the better electrocatalytic kinetics of the former [47]. The Mott-Schottky plots in Fig. S10 confirm that Cu<sub>2</sub>O and TiO<sub>2</sub> are p-type and n-type semiconductors, respectively (Mott-Schottky slope of greater or less than zero is the respective property of n-type and p-type semiconductor) [48,49]. The successful construction of p-n heterojunction contributes to the reduction of charge transfer resistance [48]. According to the double layer

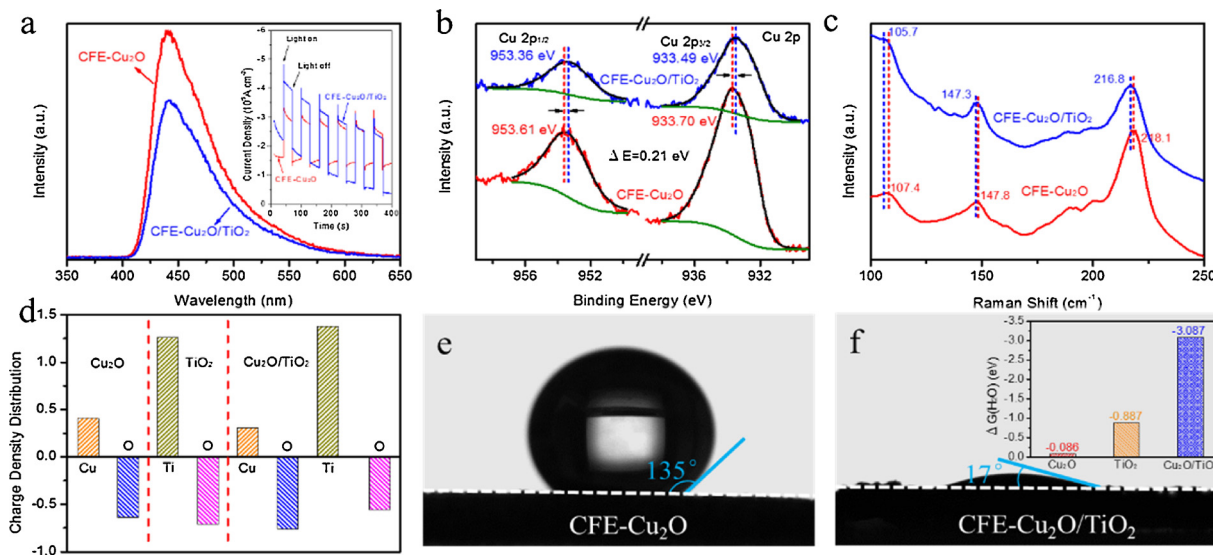


**Fig. 3.** PL spectra (a), photocurrent (inset of a), Cu 2p XPS spectra (b) and Raman spectra (c) of CFE-Cu<sub>2</sub>O and CFE-Cu<sub>2</sub>O/TiO<sub>2</sub>. (d) The charge density distribution of Cu<sub>2</sub>O, TiO<sub>2</sub> and Cu<sub>2</sub>O/TiO<sub>2</sub>. The contact angles of a drop of H<sub>2</sub>O on CFE-Cu<sub>2</sub>O (e) and CFE-Cu<sub>2</sub>O/TiO<sub>2</sub> (f). Inset of (f) is the calculated free energy for the adsorption of H<sub>2</sub>O on Cu<sub>2</sub>O, TiO<sub>2</sub> and Cu<sub>2</sub>O/TiO<sub>2</sub>.

capacitance of electrodes, the electrochemical active surface area values ( $S_{ESA}$ ) of CF, CFE-Cu<sub>2</sub>O, and CFE-Cu<sub>2</sub>O/TiO<sub>2</sub> can be calculated [46]. CFE-Cu<sub>2</sub>O/TiO<sub>2</sub> exhibits the largest  $S_{ESA}$ , suggesting that TiO<sub>2</sub> in CFE-Cu<sub>2</sub>O/TiO<sub>2</sub> plays a determining role in the HER process (Fig. S11).

The electrocatalytic activity of CF, CFE-TiO<sub>2</sub>, CFE-Cu<sub>2</sub>O and CFE-Cu<sub>2</sub>O/TiO<sub>2</sub> is tested in alkaline medium (1.0 mol L<sup>-1</sup> KOH) without iR correction, to get closer to the practical situation. The modification for

CF each time significantly promotes HER acceleration.

As seen in Fig. 4b, HER onset potential at CFE-Cu<sub>2</sub>O/TiO<sub>2</sub> is close to 18 mV, which is below than those of CF (65 mV), CFE-TiO<sub>2</sub> (60 mV) and CFE-Cu<sub>2</sub>O (27 mV). The potential of CFE-Cu<sub>2</sub>O/TiO<sub>2</sub> (114 mV) at a current density of 10 mA cm<sup>-2</sup> also is much smaller than that required of CF (408 mV), CFE-TiO<sub>2</sub> (303 mV) and CFE-Cu<sub>2</sub>O (179 mV). At the same potentials, CFE-Cu<sub>2</sub>O/TiO<sub>2</sub> can maintain higher current densities

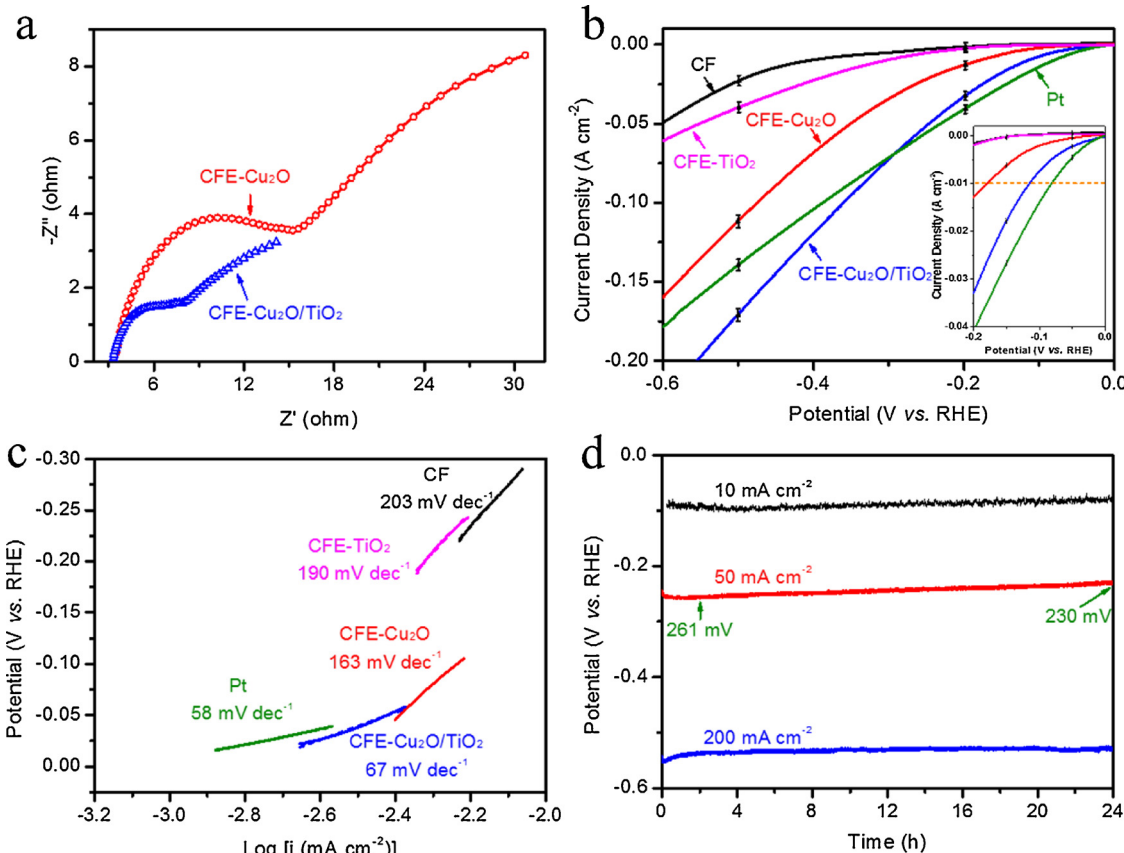


**Fig. 4.** (a) Nyquist plots of CFE-Cu<sub>2</sub>O and CFE-Cu<sub>2</sub>O/TiO<sub>2</sub>. Polarization curves (b) and Tafel slope (c) of CF, CFE-TiO<sub>2</sub>, CFE-Cu<sub>2</sub>O, CFE-Cu<sub>2</sub>O/TiO<sub>2</sub> and Pt. (d) Chronoamperometry measurements of CFE-Cu<sub>2</sub>O/TiO<sub>2</sub> at the various current densities for 24 h.

compared to those of CF and CFE-Cu<sub>2</sub>O (such as the potentials at 0.1, 0.2 and 0.3 V). For comparison, the polarization curves with IR correction also are provided in Fig. S12. The overpotential with IR correction of CFE-Cu<sub>2</sub>O/TiO<sub>2</sub> at 10 mA cm<sup>-2</sup> is 96 mV, still smaller than that of CFE-Cu<sub>2</sub>O (160 mV).

It should be noted that the electrocatalytic activity of CFE-Cu<sub>2</sub>O/TiO<sub>2</sub> is only slightly weaker than that of Pt mesh (onset potential of 0 mV, potential of 82 mV at 10 mA cm<sup>-2</sup>). The catalytic activity of CFE-Cu<sub>2</sub>O is superior to that of CF-Cu<sub>2</sub>O (Fig. S13). Furthermore, the treatment times has an obvious effect on the HER activity of the CFE-Cu<sub>2</sub>O/TiO<sub>2-x</sub> (x denotes for the treatment times). The catalytic activity of CFE-Cu<sub>2</sub>O/TiO<sub>2</sub> (i.e., CFE-Cu<sub>2</sub>O/TiO<sub>2-3</sub>) exceeds those of CF-Cu<sub>2</sub>O/TiO<sub>2-3</sub>, CFE-Cu<sub>2</sub>O/TiO<sub>2-1</sub> and CFE-Cu<sub>2</sub>O/TiO<sub>2-5</sub>, suggesting that the chemical erosion for CF and the moderate amounts of TiO<sub>2</sub> have an obvious impact on the electrocatalytic activity of electrode (Fig. S14). The HER performance of CFE-TiO<sub>2</sub> is close to that of CFE, indicating the weak catalytic performance of pure TiO<sub>2</sub> (Fig. 4b). Besides, by comparison with the other electrocatalysts recently reported (Table S1), the HER catalytic activity of CFE-Cu<sub>2</sub>O/TiO<sub>2</sub> is better than those of most electrocatalysts in alkaline medium and even comparable to those of electrocatalysts in acidic medium. From Fig. 4c it can also be seen that CFE-Cu<sub>2</sub>O/TiO<sub>2</sub> (67 mV dec<sup>-1</sup>) shows the smallest Tafel slope with respect to the ones of CF (203 mV dec<sup>-1</sup>), CFE-TiO<sub>2</sub> (190 mV dec<sup>-1</sup>) and CFE-Cu<sub>2</sub>O (163 mV dec<sup>-1</sup>), indicating the much more favorable kinetics of CFE-Cu<sub>2</sub>O/TiO<sub>2</sub> for the HER.

To evaluate the long-term electrochemical stability of monolithic CFE-Cu<sub>2</sub>O/TiO<sub>2</sub>, the chronoamperometry experiments are successively performed at current density values of 10, 50, and 200 mA cm<sup>-2</sup> for 24 h. After a small initial fluctuation, the potentials can remain stable and even slightly reduce, as seen in Fig. 4d. For example, the potentials after the stability test of 2 and 24 h at the current density of 50 mA cm<sup>-2</sup> are 261 and 230 mV, indicating the improved electrochemical activity during the stability test. The polarization curves after the stability tests at different current densities are also recorded (Fig. 5a).

The gradually improved polarization curves can be observed along with the stability tests (Fig. 5a). The physical and chemical properties of monolithic CFE-Cu<sub>2</sub>O/TiO<sub>2</sub> after stability tests are detected to further prove its outstanding electrochemical durability. The SEM image shows

that the small particles of TiO<sub>2</sub> still closely combine with the surface of electrodes and a small number of cracks resulting from the impact of the generation of many bubbles can be seen (Fig. 5b). EDX mappings reveal the uniform distribution of O, Cu and Ti and the elemental composition before and after stability tests remains unchanged according to XPS survey spectra of CFE-Cu<sub>2</sub>O/TiO<sub>2</sub> (Figs 5c and S15). No existence of Pt 5p<sub>1/2</sub> (51.5 eV), Pt 5p<sub>3/2</sub> (66.0 eV), Pt 4f<sub>7/2</sub> (71.0 eV) and Pt 4f<sub>5/2</sub> (74.4 eV) and Pt 5s (102.0 eV) signals is found in CFE-Cu<sub>2</sub>O/TiO<sub>2</sub> after the stability test [50]. This indicates that Pt ions are not adsorbed on the working electrode during the electrochemical tests. The weakened characteristic peaks in XRD pattern and the existence of Ti<sup>+3</sup> peaks in high resolution Ti 2p XPS spectra demonstrate the reduced crystallinity of CFE-Cu<sub>2</sub>O/TiO<sub>2</sub>, originating from the electro-reduction process (Figs 5d and S16). After the stability tests, the charge transfer resistance of CFE-Cu<sub>2</sub>O/TiO<sub>2</sub> is reduced from 6.0 to 0.2 Ω (Fig. 5e). When a drop of water hits on the surface of dried electrode after tests, the droplet will be absorbed quickly, indicating the improved hydrophilicity (Fig. 5f). The enhanced conductivity and the negligible contact angle between water and electrode, after the stability test, are responsible for the reduced potentials in long-term durability process (Figs 5e and f).

### 3.3. Discussion

Based on the above analysis, the illustrations of the space-charge region formation and the charges distribution change for the monolithic CFE-Cu<sub>2</sub>O/TiO<sub>2</sub> are schematically exhibited in Figs 6 a and b.

The n-type TiO<sub>2</sub> and p-type Cu<sub>2</sub>O carry negative and positive charges. When the formation of p-n heterojunction is accomplished, in the contact zone of TiO<sub>2</sub> and Cu<sub>2</sub>O, the Fermi levels difference drive the flow of the charges until balance [29]. At this point, the local areas of Cu<sub>2</sub>O and TiO<sub>2</sub> carry many negative and positive charges respectively, resulting in the generation of space-charge regions (contact potentials) followed by the electric field formation from TiO<sub>2</sub> to Cu<sub>2</sub>O and the band bending (Figs 6a and 6b) [29,32,51]. This charge density change in heterojunction is consistent with the above presented experimental results and the theoretical calculations. Thus, many active sites are formed at interface and many electrons from bias will be consumed

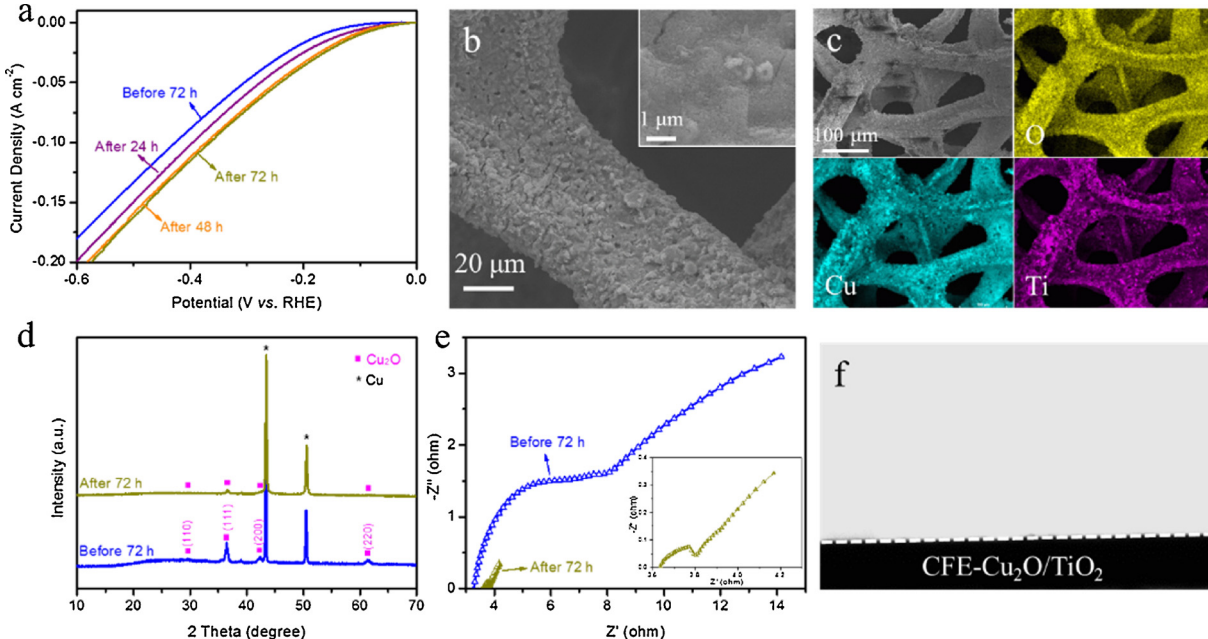


**Fig. 5.** (a) Polarization curves of CFE-Cu<sub>2</sub>O/TiO<sub>2</sub> after stability test. (b) SEM images of CFE-Cu<sub>2</sub>O/TiO<sub>2</sub> after stability test. (c) Elemental mappings of CFE-Cu<sub>2</sub>O/TiO<sub>2</sub> after stability test. (d) XRD patterns of CFE-Cu<sub>2</sub>O/TiO<sub>2</sub> before and after stability test. (e) Nyquist plots of CFE-Cu<sub>2</sub>O/TiO<sub>2</sub> before and after stability test. (f) The contact angle of a drop of H<sub>2</sub>O on CFE-Cu<sub>2</sub>O/TiO<sub>2</sub> after stability test.

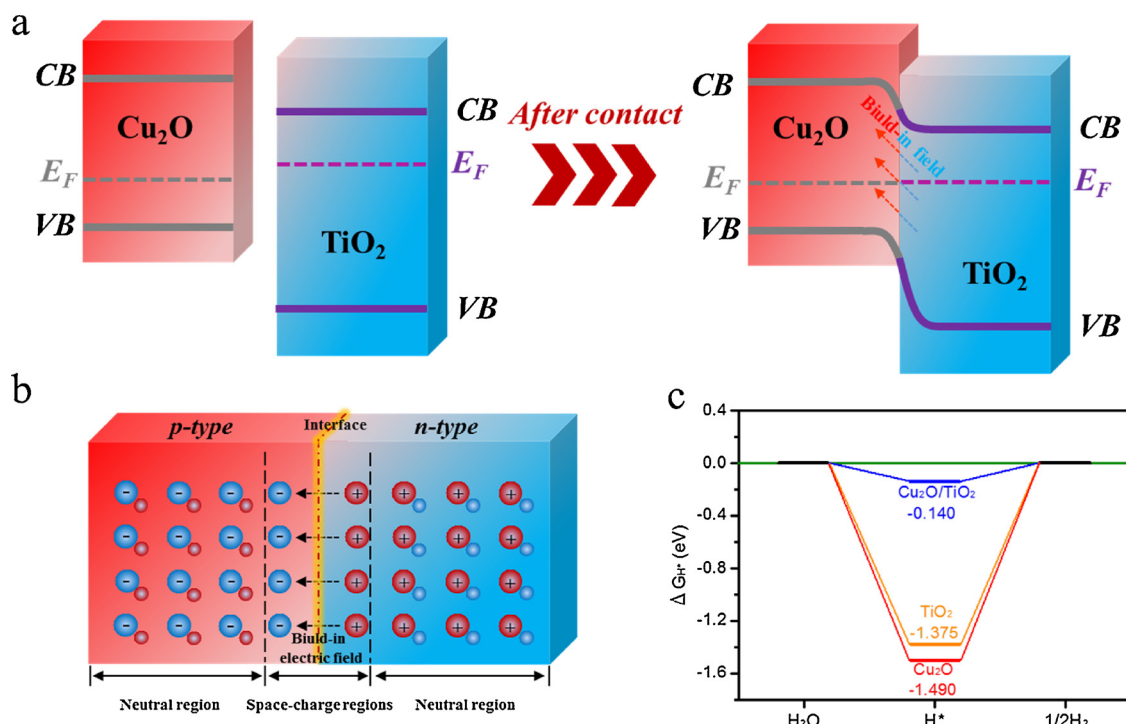


**Fig. 6.** (a) Energy band diagram of Cu<sub>2</sub>O and TiO<sub>2</sub> before and after contact. (b) Schematic illustration of space-charge region at the contact zone of p-type Cu<sub>2</sub>O and n-type TiO<sub>2</sub> heterojunction. (c) H adsorption free energy profiles of Cu<sub>2</sub>O, TiO<sub>2</sub> and Cu<sub>2</sub>O/TiO<sub>2</sub>.

here [12,29]. The p-n heterojunction is beneficial to the electron transfer from Cu<sub>2</sub>O to TiO<sub>2</sub>, leading to further HER on TiO<sub>2</sub>. The improved Volmer step has been verified in previous analysis. To further speed up the HER dynamics, the improvement of Heyrovsky step is necessary. According to DFT calculations, the H adsorption free energy value is −1.490 eV on Cu<sub>2</sub>O and −1.375 eV on TiO<sub>2</sub>; such strong adsorption for H can hinder the Heyrovsky step (Fig. 6c) [29,46].

However, the formation of Cu<sub>2</sub>O/TiO<sub>2</sub> heterojunction can markedly increase the adsorption free energy of H and its value approaches 0 eV. This is ascribed to the changed electrons density in heterojunction, improving the combination between active-sites and H; fact that explains the observed superior HER performance of CFE-Cu<sub>2</sub>O/TiO<sub>2</sub> [29,46].

#### 3.4. Scale-up experiment

The CFE-Cu<sub>2</sub>O/TiO<sub>2</sub> preparation process is so simple that its large-scale fabrication can be enabled. A large area CFE-Cu<sub>2</sub>O/TiO<sub>2</sub> (10.0 cm × 10.0 cm, denoted CFE-Cu<sub>2</sub>O/TiO<sub>2</sub>-S) can be obtained as seen in Fig. 7a.

There is no obvious difference in compositions and morphologies between CFE-Cu<sub>2</sub>O/TiO<sub>2</sub> and CFE-Cu<sub>2</sub>O/TiO<sub>2</sub>-S, suggesting its feasibility of large-scale preparation (Figs. S17, S18 and 7b). Moreover, two pieces of samples (1.0 cm × 2.0 cm) (CFE-Cu<sub>2</sub>O/TiO<sub>2</sub>-S1 and CFE-Cu<sub>2</sub>O/TiO<sub>2</sub>-S2) were cut from CFE-Cu<sub>2</sub>O/TiO<sub>2</sub>-S, tested for HER under the same conditions as those of CFE-Cu<sub>2</sub>O/TiO<sub>2</sub>.

Their polarization curves almost overlap (Fig. 7c), demonstrating the successful scale-up fabrication of CFE-Cu<sub>2</sub>O/TiO<sub>2</sub> with excellent HER activity.

Owing to its outstanding flexibility, CFE-Cu<sub>2</sub>O/TiO<sub>2</sub>-S can be folded into the fixed shape as displayed in Fig. 7d. To present the application of commercial electrode, a simulative three electrode system with CFE-Cu<sub>2</sub>O/TiO<sub>2</sub>-S as working electrode is set up (Fig. 7e).

#### 4. Conclusions

In conclusion, a well-designed monolithic etched copper foam-based Cu<sub>2</sub>O layer decorated with TiO<sub>2</sub> nanodots heterojunction electrocatalyst is prepared and tested, exhibiting superior HER in alkaline solution. The increased specific surface area and pore volume of etched copper foam leads to the exposure of more active sites. The modification of TiO<sub>2</sub>, with excellent hydrophilicity, for Cu<sub>2</sub>O reduces electron transfer resistance and H<sub>2</sub>O adsorption free energy, weakening as a consequence the H adsorption on CFE-Cu<sub>2</sub>O/TiO<sub>2</sub>. The space-charge region of p-n heterojunction prompts the increased electron density on the local area of Cu<sub>2</sub>O, leading to the rich electrons in active sites. Therefore, CFE-Cu<sub>2</sub>O/TiO<sub>2</sub> exhibits an outstanding electrocatalytic activity (HER onset potential: 18 mV, potential: 114 mV@10 mA cm<sup>−2</sup>, Tafel slope: 67 mV dec<sup>−1</sup>) and long-term stability (almost no fading after the stability test for 72 h). It is believed that this work will provide a new idea for designing electrochemical water splitting electrocatalysts consisting of semiconductors.

#### Acknowledgment

This work is supported by the National Science Fund for Distinguished Young Scholars (21425627), the Natural Science Foundation of China (21476271, 21461162003, 21576299, 21576300 and 21773315), the Science and Technology Plan Project of Guangdong Province (2017A050501009) and the Fundamental Research Funds for the Central Universities (17lgjc36, 17lgzd14), Nature Science Foundation of Guangdong Province (2014A030313150), Tip-top Scientific and Technical Innovative Youth Talents of Guangdong special support program (2016QT03N322), Guangzhou Science and Technology Project (201607010104, 201707010079) and the Local Innovative and Research Teams Project of Guangdong Pearl River Talents Program (201804020025). Prof. Tsiaikaras has been financially supported by the Ministry of Education and Science of the Russian Federation (Mega-Grant, contract no. 14.Z50.31.0001) and co-financed by the European Union and Greek national funds through the

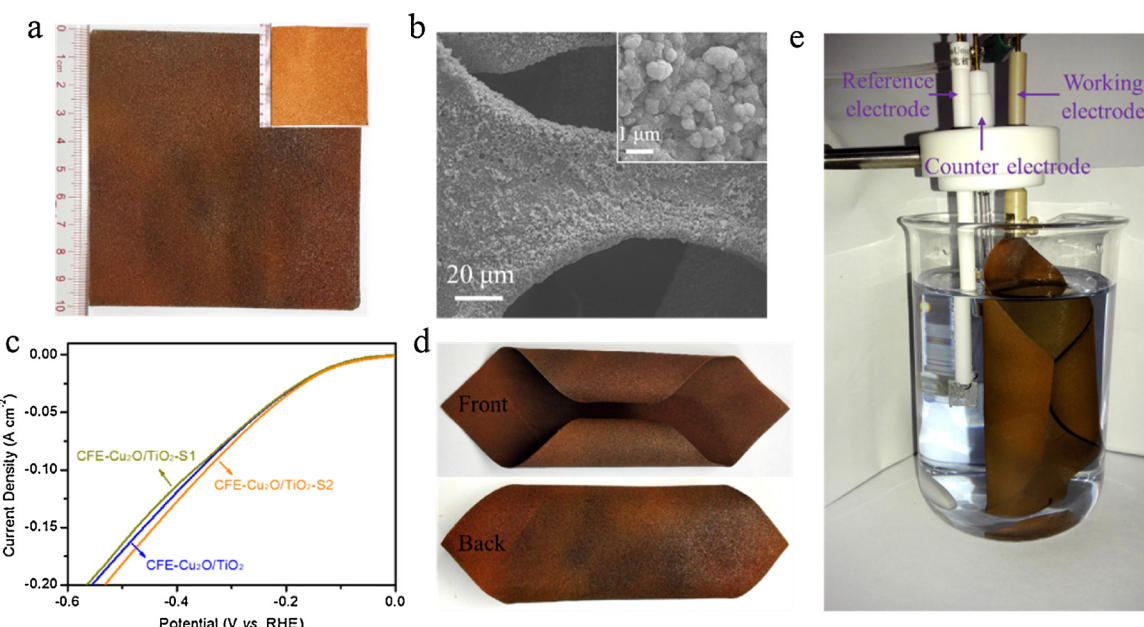


**Fig. 7.** (a) Digital photograph of CFE-Cu<sub>2</sub>O/TiO<sub>2</sub>-S (10.0 cm × 10.0 cm) and inset is untreated CF. (b) SEM images of CFE-Cu<sub>2</sub>O/TiO<sub>2</sub>-S. (c) Polarization curves of CFE-Cu<sub>2</sub>O/TiO<sub>2</sub>, CFE-Cu<sub>2</sub>O/TiO<sub>2</sub>-S1 and CFE-Cu<sub>2</sub>O/TiO<sub>2</sub>-S2. (d) Digital photograph of CFE-Cu<sub>2</sub>O/TiO<sub>2</sub>-S shaped into a specific shape. (e) Digital photograph of HER equipment using CFE-Cu<sub>2</sub>O/TiO<sub>2</sub>-S, Pt and Ag/AgCl as working electrode, counter electrode and reference electrode and electrolyte is 1 M KOH.

Operational Program Competitiveness, Entrepreneurship and Innovation, under the call RESEARCH – CREATE – INNOVATE (project code:T1EDK-02442).

## Appendix A. Supplementary data

Supplementary material related to this article can be found, in the online version, at doi:<https://doi.org/10.1016/j.apcatb.2018.10.039>.

## References

- [1] D. Akyuz, B. Keskin, U. Sahinturk, A. Koca, *Appl. Catal. B: Environ.* 188 (2016) 217–226.
- [2] Z. Pu, S. Wei, Z. Chen, S. Mu, *Appl. Catal. B: Environ.* 196 (2016) 193–198.
- [3] C. Canales, F. Varas-Concha, T.E. Mallouk, G. Ramírez, *Appl. Catal. B: Environ.* 188 (2016) 169–176.
- [4] Y. Xu, M. Kraft, R. Xu, *Chem. Soc. Rev.* 45 (2016) 3039.
- [5] R. He, J. Hua, A. Zhang, C. Wang, J. Peng, W. Chen, J. Zeng, *Nano Lett.* 17 (2017) 4311–4316.
- [6] Y.J. Ko, J.M. Cho, I. Kim, D.S. Jeong, K.S. Lee, J.K. Park, Y.J. Baik, H.J. Choi, W.S. Lee, *Appl. Catal. B: Environ.* 203 (2016) 684–691.
- [7] S. Gupta, N. Patel, R. Fernandes, R. Kadrekar, A. Dashora, A.K. Yadav, D. Bhattacharyya, S.N. Jha, A. Miottello, D.C. Kothari, *Appl. Catal. B: Environ.* 192 (2016) 126–133.
- [8] H. Xu, J.-X. Feng, Y.-X. Tong, G.-R. Li, *ACS Catal.* 7 (2016) 986–991.
- [9] J. Zhao, P.D. Tran, Y. Chen, J.S.C. Loo, J. Barber, Z.J. Xu, *ACS Catal.* 5 (2015) 4115–4120.
- [10] P. Xiao, Y. Yan, X. Ge, Z. Liu, J.Y. Wang, X. Wang, P. Xiao, Y. Yan, X. Ge, Z. Liu, *Appl. Catal. B: Environ.* 154–155 (2014) 232–237.
- [11] K. Xu, H. Cheng, H. Lv, J. Wang, L. Liu, S. Liu, X. Wu, W. Chu, C. Wu, Y. Xie, *Adv. Mater.* 30 (2018) 1703322.
- [12] J. Zhang, T. Wang, D. Pohl, B. Rellinghaus, R. Dong, S. Liu, X. Zhuang, X. Feng, *Angew. Chem.* 55 (2016) 6702–6707.
- [13] A.M. Gómez-Marin, E.A. Ticianelli, *Appl. Catal. B: Environ.* 209 (2017) 600–610.
- [14] M.-S. Balogun, W. Qiu, H. Yang, W. Fan, Y. Huang, P. Fang, G. Li, H. Ji, Y. Tong, *Energy Environ. Sci.* 9 (2016) 3411–3416.
- [15] C. Hahn, T. Hatsukade, Y.-G. Kim, A. Vailionis, J.H. Baricuatro, D.C. Higgins, S.A. Nitopi, M.P. Soriaga, T.F. Jaramillo, *Proc. Natl. Acad. Sci. U. S. A.* 114 (2017) 5918–5923.
- [16] X. Wang, X. Gan, T. Hu, K. Fujisawa, Y. Lei, Z. Lin, B. Xu, Z.H. Huang, F. Kang, M. Terrones, R. Lv, *Adv. Mater.* 29 (2017) 1603617.
- [17] R. Liu, Y. Wang, D. Liu, Y. Zou, S. Wang, *Adv. Mater.* 29 (2017) 1701546.
- [18] X. Zhang, X. Yu, L. Zhang, F. Zhou, Y. Liang, R. Wang, *Adv. Funct. Mater.* (2018) 1706523.
- [19] L. Zhang, J. Lu, S. Yin, L. Luo, S. Jing, A. Brouzgou, J. Chen, P.K. Shen, P. Tsiaikaras, *Appl. Catal. B: Environ.* 230 (2018) 58–64.
- [20] C. Li, S. Wang, T. Wang, Y. Wei, P. Zhang, J. Gong, *Small* 10 (2014) 2741.
- [21] J. Tian, Q. Liu, N. Cheng, A.M. Asiri, X. Sun, *Angew. Chem.* 53 (2014) 9577–9581.
- [22] Y. Deng, A.D. Handoko, Y. Du, S. Xi, B.S. Yeo, *ACS Catal.* 6 (2016) 2473–2481.
- [23] M. Kuang, P. Han, Q. Wang, J. Li, G. Zheng, *Adv. Funct. Mater.* 26 (2016) 8555.
- [24] L. Yu, H. Zhou, J. Sun, F. Qin, D. Luo, L. Xie, F. Yu, J. Bao, Y. Li, Y. Yu, S. Chen, Z. Ren, *Nano Energy* 41 (2017) 327–336.
- [25] M. Jahan, Z. Liu, K.P. Loh, *Adv. Funct. Mater.* 23 (2013) 5363–5372.
- [26] J.X. Feng, J.Q. Wu, Y. Tong, G.R. Li, *J. Am. Chem. Soc.* 140 (2017) 610–617.
- [27] P. Chen, K. Xu, S. Tao, T. Zhou, Y. Tong, H. Ding, L. Zhang, W. Chu, C. Wu, Y. Xie, *Adv. Mater.* 28 (2016) 7527.
- [28] Z.H. Xiao, Y. Wang, Y.C. Huang, Z.X. Wei, C.L. Dong, J.M. Ma, S.H. Shen, Y.F. Li, S.Y. Wang, *Environ. Energy Sci.* 10 (2017) 2563–2569.
- [29] Z. Zhuang, Y. Li, Z. Li, F. Lv, Z. Lang, K. Zhao, L. Zhou, L. Moskaleva, S. Guo, L. Mai, *Angew. Chem.* 57 (2018) 496–500.
- [30] H. Li, Z. Yang, J. Zhang, Y. Huang, H. Ji, Y. Tong, *Appl. Surf. Sci.* 423 (2017) 1188–1197.
- [31] K.H. Ye, Z. Chai, J. Gu, X. Yu, C. Zhao, Y. Zhang, W. Mai, *Nano Energy* 18 (2015) 222–231.
- [32] W. Qiu, Y. Huang, S. Tang, H. Ji, Y. Tong, *J. Phys. Chem. C* 121 (2017) 17150–17159.
- [33] M. Machida, K. Norimoto, T. Watanabe, K. Hashimoto, A. Fujishima, *J. Mater. Sci.* 34 (1999) 2569–2574.
- [34] R. Fateh, R. Dillert, D. Bahnemann, *Langmuir* 29 (2013) 3730–3739.
- [35] Y. Wei, X. Chang, T. Wang, C. Li, J. Gong, Y. Wei, X. Chang, T. Wang, C. Li, J. Gong, *Small* 13 (2017) 1702007.
- [36] M. Gao, W. Sheng, Z. Zhuang, Q. Fang, S. Gu, J. Jiang, Y. Yan, *J. Am. Chem. Soc.* 136 (2014) 7077–7084.
- [37] K. Xu, P. Chen, X. Li, Y. Tong, H. Ding, X. Wu, W. Chu, Z. Peng, C. Wu, Y. Xie, *J. Am. Chem. Soc.* 137 (2015) 4119–4125.
- [38] M.-S. Balogun, C. Li, Y. Zeng, M. Yu, Q. Wu, M. Wu, X. Lu, Y. Tong, *J. Power Sources* 272 (2014) 946–953.
- [39] V. Scuderi, G. Impellizzeri, M. Zimbone, R. Sanz, A. Di Mauro, M.A. Buccheri, M. Mirtillo, A. Terrasi, G. Rappazzo, G. Nicotra, V. Privitera, *Appl. Catal. B: Environ.* 183 (2016) 328–334.
- [40] Y. Huang, W. Fan, B. Long, H. Li, W. Qiu, F. Zhao, Y. Tong, H. Ji, *J. Mater. Chem. A* 4 (2016) 3648–3654.
- [41] T. Choudhury, S.O. Saied, J.L. Sullivan, A.M. Abbot, *J. Phys. D Appl. Phys.* 22 (1989) 1185.
- [42] K. Yuan, Q. Cao, X. Li, H.Y. Chen, Y. Deng, Y.Y. Wang, W. Luo, H.L. Lu, D.W. Zhang, *Nano Energy* 14 (2017) 543–551.
- [43] W. Fan, C. Li, H. Bai, Y. Zhao, B. Luo, Y. Li, Y. Ge, W. Shi, H. Li, *J. Mater. Chem. A* 5 (2017) 4894–4903.
- [44] G. Wang, X. Xiao, W. Li, Z. Lin, Z. Zhao, C. Chen, C. Wang, Y. Li, X. Huang, L. Miao, C. Jiang, Y. Huang, X. Duan, *Nano Lett.* 15 (2015) 4692–4698.
- [45] Y. Mao, T. He, X. Sun, W. Li, X. Lu, J. Gan, Z. Liu, L. Gong, J. Chen, P. Liu, Y. Tong, *Electrochim. Acta* 62 (2012) 1–7.
- [46] J.X. Feng, H. Xu, Y.T. Dong, X.F. Lu, Y.X. Tong, G.R. Li, *Angew. Chem.* 129 (2017) 3006–3010.
- [47] J.X. Feng, H. Xu, S.H. Ye, G. Ouyang, Y.X. Tong, G.R. Li, *Angew. Chem.* 56 (2017) 8120–8124.
- [48] B. Long, M.-S. Balogun, L. Luo, W. Qiu, Y. Luo, S. Song, Y. Tong, *Adv. Energy Mater.* 8 (2018) 1701681.
- [49] Y. Huang, H. Li, M.-S. Balogun, W. Liu, Y. Tong, X. Lu, H. Ji, *ACS Appl. Mater. Interfaces* 6 (2014) 22920–22927.
- [50] M.J.H. Rodríguez, E.P. Melián, D.G. Santiago, O.G. Díaz, J.A. Navío, J.M.D. Rodríguez, *Appl. Catal. B: Environ.* 205 (2017) 148–157.
- [51] M. Xie, X. Fu, L. Jing, P. Luan, Y. Feng, H. Fu, *Adv. Energy Mater.* 4 (2014) 1300995.